Theor Appl Climatol
DOI 10.1007/s00704-017-2138-1

ORIGINAL PAPER

Characteristics of southern California atmospheric rivers

Sarah M. Harris[1] · **Leila M. V. Carvalho**[1,2]

Received: 29 August 2016 / Accepted: 23 April 2017

Abstract Atmospheric rivers (ARs) are channels of high water vapor flux that transport moisture from low to higher latitudes on synoptic timescales. In areas of topographical variability, ARs may lead to high-intensity precipitation due to orographic forcing. ARs landfalling along North America's west coast are linked to extreme events including those leading to flooding and landslides. In southern California (SCA), proper AR forecasting is important for regional water resources as well as hazard mitigation and as the area's annual precipitation totals occur from relatively few storms per season, any changes to storm frequency and/or intensity may have dramatic consequences. Yet, as most regional AR studies focus on the Pacific Northwest, there is little information about SCA ARs. We develop an algorithm to identify ARs landfalling on North America's west coast between 1979 and 2013 within total precipitable water reanalysis fields. ARs are then categorized according to landfall region. To determine and differentiate the characteristics and spatial distributions of ARs affecting these areas, we examine lag composites of various atmospheric variables for each landfall region. SCA ARs differ from ARs landfalling farther north in the days prior to landfall with the position and amplitude of a trough offshore from the Asian continent and ridge over Alaska, as well as the displacement and eastward extension of the jet core that potentially guides AR moisture southwards. The relationships between AR landfalls and the El Niño/Southern Oscillation (ENSO), the Madden-Julian Oscillation (MJO), and the Pacific/North American Teleconnection Pattern (PNA) are also investigated.

1 Introduction

In most of southern California (SCA), the total annual precipitation is attained from relatively few storms that follow a defined seasonal regime (Dettinger et al. 2011). Storm intensity and frequency can dramatically affect the region because the landscape is prone to several rainfall-induced hazardous events, such as flooding and landslides (e.g., Caine 1980). These events cause significant damage to properties and frequently take human lives. Many local industries including tourism and agriculture are intrinsically linked to an area's climate and thus, are affected by extreme meteorological events. Additionally, SCA is currently experiencing one of the most severe droughts on record and the future of regional water resources may depend on a handful of extreme storms. Understanding what causes precipitation variability is essential for accurate storm forecasting, water management, and mitigation against hazards in SCA.

Excessive daily rainfall in SCA has been associated with bands of enhanced water vapor known as atmospheric rivers (ARs) (e.g., Dettinger et al. 2011; Kim et al. 2013; Rutz and Steenburgh 2012). On synoptic timescales ARs are long (≥2000 km), narrow (≤1000 km) channels of high water vapor flux found within the low troposphere (Neiman et al. 2008a, b; Ralph et al. 2005, 2006, 2010; Zhu and Newell 1994, 1998) and are comparable to water vapor "highways." ARs are responsible for most of the planet's meridional water vapor movement (>90%) even while covering a small (<10%) percentage of Earth's surface (Neiman et al. 2008a; Ralph et al. 2004; Zhu and Newell 1994, 1998). Found within the pre-cold frontal warm sectors of extratropical cyclones (Bao et al.

✉ Sarah M. Harris
sarah.harris@geog.ucsb.edu

[1] Department of Geography, University of California, Santa Barbara, 1832 Ellison Hall, Santa Barbara, CA 93106, USA

[2] Earth Research Institute, Santa Barbara, CA, USA

2006; Dettinger et al. 2011; Neiman et al. 2008a, b; Ralph et al. 2004, 2005, 2006), ARs are intrinsically linked to extratropical cyclone activity and bear a resemblance to low-level jets. AR moisture sources differ in that some events occur with direct transport of water vapor from tropical sources to midlatitudes with few losses of water vapor due to precipitation (e.g., Bao et al. 2006; Knippertz and Martin 2007; Ralph et al. 2010). Other events suggest a continuous cycling of water vapor with local moisture sources from convergence, particularly along the cold fronts of extratropical cyclones that contribute to AR maintenance and formation (Bao et al. 2006; Newman et al. 2012; Sodemann and Stohl 2013).

AR cores exhibit warm temperatures, high water vapor content, as well as strong winds organized as wind jets resulting in high water vapor flux (Dettinger et al. 2011; Neiman et al. 2008a; Ralph and Dettinger 2011, 2012; Ralph et al. 2004, 2005). Most of the water vapor transport occurs in the lowest 2.5 km of the troposphere, in an area that has weak moist static stability (Neiman et al. 2008a; Ralph and Dettinger 2012; Ralph et al. 2004, 2005, 2006; Sodemann and Stohl 2013). When ARs encounter coastal mountain ranges, high-intensity rainfall can occur due to uplift of this warm, water vapor dense air along mountain slopes (Neiman et al. 2002, 2008a; Ralph and Dettinger 2011, 2012; Ralph et al. 2005).

North America's west coast is one such region that experiences extreme orographic precipitation due to AR activity (e.g., Neiman et al. 2008b; Ralph and Dettinger 2012); however, AR-induced rainfall varies by latitude as well as coastal and inland regions (Kim et al. 2013; Neiman et al. 2008a, b; Rutz et al. 2014, 2015). AR storms affecting this area form over the Pacific Ocean and are generally characterized by an offshore trough that varies in depth and location depending on the AR landfall area (Neiman et al. 2008a,b). In this region, ARs are linked with high-intensity precipitation resulting in flooding as well as changes to regional snowpack totals (e.g., Neiman et al. 2011; Guan et al. 2013). AR-induced rainfall is strongest along the coast and weakens upon moving inland, particularly if an AR crosses a mountain barrier; however, ARs that produce precipitation over inland areas have the highest moisture contents and/or strongest winds of all ARs (Rutz et al. 2015). While the characteristics of ARs affecting North America's west coast are generally understood and well examined (e.g., Neiman et al. 2008a), the characteristics and mechanisms of those affecting SCA have not been thoroughly investigated yet.

Along the North American coastline, ARs most frequently landfall in northern latitudes and occur at a lesser frequency in SCA (e.g., Neiman et al. 2008a, b; Rutz et al. 2014). Nonetheless, SCA AR events are responsible for some of the area's highest-intensity precipitation (Dettinger et al. 2011; Kim et al. 2013; Neiman et al. 2008a). For this region, the highest AR frequencies occur during Boreal winter as this is when extratropical cyclones associated with AR initiation and maintenance are also more frequent (Kim et al. 2013; Neiman et al. 2008a; Rutz and Steenburgh 2012). The majority of AR precipitation occurs in only a few events per season but can account for significant proportions of regional annual rainfall totals (Dettinger et al. 2011; Neiman et al. 2013; Rutz et al. 2014).

Using a combination of satellite as well as station rainfall data, Dettinger et al. (2011) determines that during 1998 to 2008 ARs landfalling on North America's west coast between 32.5° and 52.5° N latitudes contributed between 30 and 45% of rainfall in all California with SCA ranging from 20 to ~35% along the coast. In a similar analysis by Rutz and Steenburgh (2012), ARs crossing over the Baja Peninsula are also accounted for increasing the AR contributing proportion between 20 and ~40% in SCA during the cool season of November–April. With few events but high precipitation totals, ARs are often of high-intensity and/or of long duration (Rutz et al. 2014). As SCA is characterized by vast mountainous terrain, particularly along the coast, high-intensity precipitation is often associated with a landfalling AR in the area (e.g., Rutz et al. 2014).

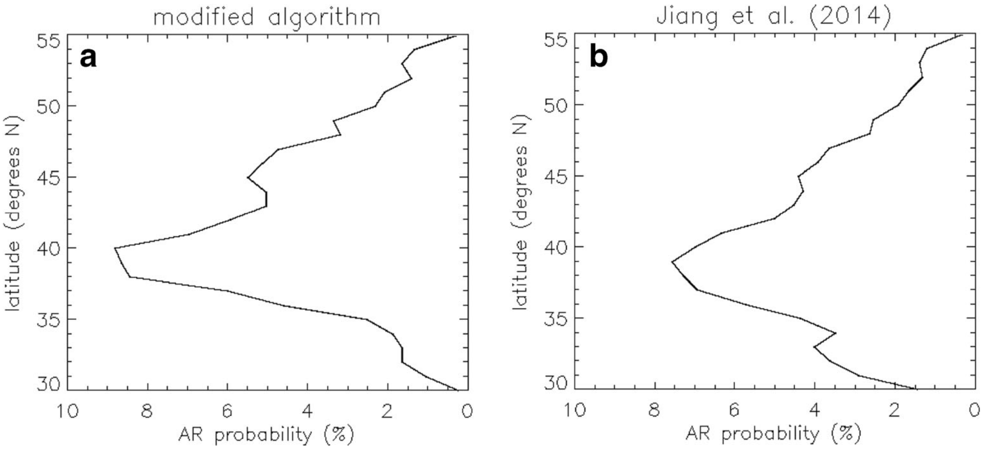

Fig. 1 Landfalling AR climatology for North America's west coast (30.0°–55.0° N) outputted from **a** the modified algorithm and from **b** the criteria described in Jiang et al. (2014). AR activity is derived using CFSR and covers DJF from 1979 to 2005

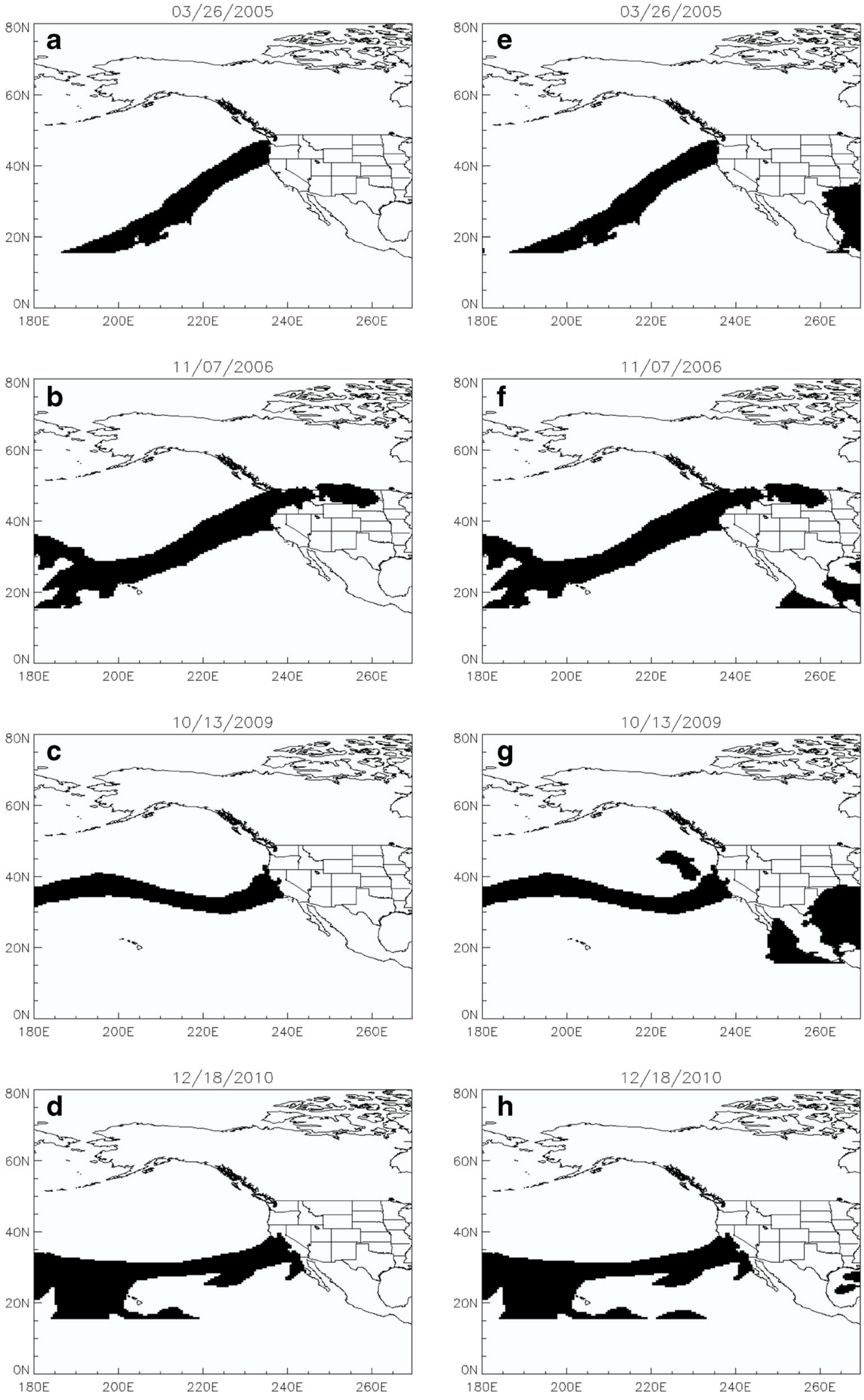

Fig. 2 AR events as identified by the algorithm presented in this paper (**a**–**d**) as well as the algorithm described in Jiang et al. 2014 (**e**–**h**) using CFSR data. Case study dates include **a**, **e** March 26, 2005, **b**, **f** November 7, 2006, **c**, **g** October 13, 2009, and **d**, **h** December 18, 2010. Areas identified as an AR are indicated by *black shading*

ARs are influenced by the interactions of tropical and extratropical phenomena. It is generally understood that the Madden-Julian Oscillation (MJO), considered the most important tropical mode on intraseasonal timescales (e.g., Madden and Julian 1994), alters North Pacific atmospheric circulation, modulating regional air and moisture movement

Table 1 Landfall regions and the number of identified landfalling ARs during Oct–Mar seasons from 1979 to 2013

Name	Abbr	Lat. covered (° N)	Landfalling ARs
Southern California	SCA	32.5°–37.0°	72
Northern California	NCA	37.0°–42.0°	213
Southern Pacific Northwest	SPNW	42.0°–47.0°	183
Northern Pacific Northwest	NPNW	47.0°–52.5°	160
All ARs	–	30.0°–55.0°	719

and affecting meteorological events that occur in North America including ARs (Bell and Higgins 2005). The propagation of the MJO's convection and associated pattern of atmospheric circulation over the Pacific and Indian Oceans (Bell and Higgins 2005; Guan et al. 2012; Mo and Higgins 1998; Ralph et al. 2010) is known to assist ARs, particularly a specific subset of ARs known as the Pineapple Express (Dettinger 2004; Dettinger et al. 2011). For seasons with frequent and/or exceptionally strong MJOs, numerous and/or higher-intensity ARs may occur causing an increase in the frequency and/or intensity of extreme precipitation events in SCA (Jones 2000; Jones et al. 2011; Payne and Magnusdottir 2014).

Payne and Magnusdottir (2014) investigate the link between MJO phases with ARs and determine that ARs affecting western North America increase in frequency during MJO phases 3, 6, 7, and 8 with the highest increase during phase 6 and the smallest increase during phase 3. This is semi-consistent with Guan et al. (2012) who compares MJO phases and AR activity to snow water equivalent (SWE) values in the Sierra Nevada and determines that positive SWE anomalies are most prominent during MJO phases 3 and 6 whereas phase 8 is associated with negative SWE anomalies.

The El Niño Southern Oscillation (ENSO) is another phenomenon known to influence precipitation in SCA through processes such as the modulation of the upper level jet and low-level moisture flux (e.g., Mo and Higgins 1998). Studies regarding ARs and ENSO reveal mixed findings. Payne and Magnusdottir (2014) determine that the frequency of landfalling ARs increases during warm ENSO phases and is

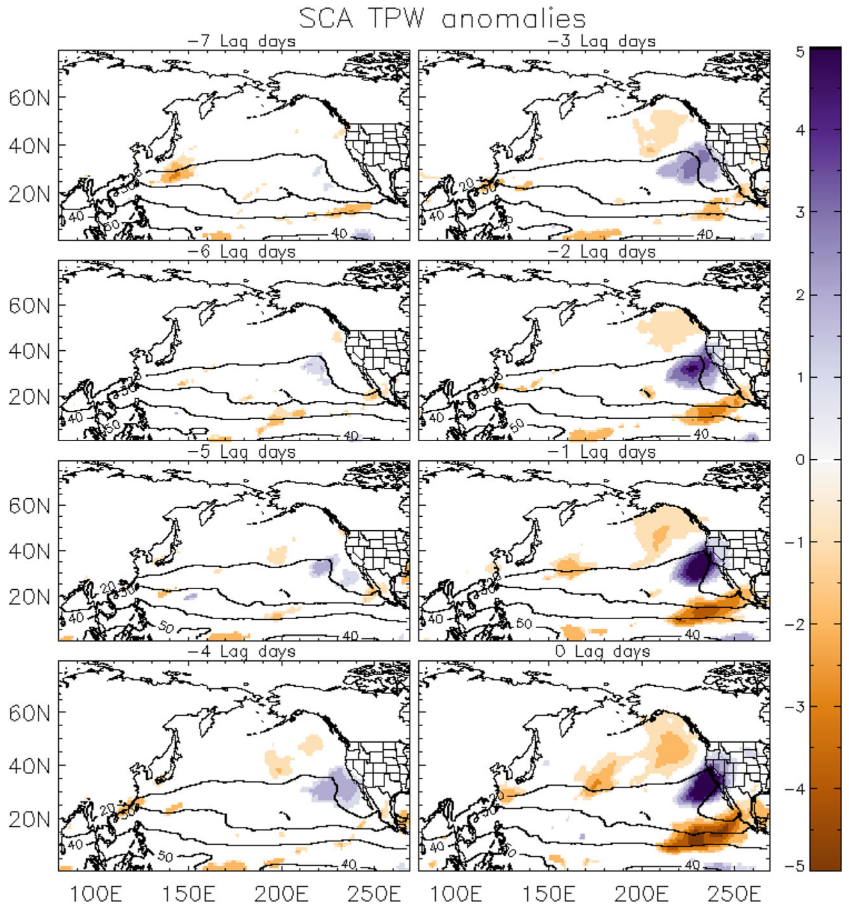

Fig. 3 Composites of TPW anomalies (*colored shading*; kg m^{-2}) overlaid with TPW (contours) starting 7 days prior to AR landfall (−7 Lag days) and continuing to the day of AR landfall (0 Lag days) for ARs affecting SCA. Anomalies are calculated at the 95% level using a Student's *t* test. TPW contours indicate regions of high moisture and begin at 20 kg m^{-2} with a contour interval of 10

at a minimum during cold ENSO phases. They also find that AR landfall latitudes shift southward during warm ENSO events. Bao et al. (2006) argue that direct “river-like” transport of moisture is most likely to occur during ENSO neutral years and least likely during warm ENSO years. Like most AR studies, investigations of the relationships between ARs and the MJO as well as ENSO is limited to AR events affecting northern latitudes or the west coast of North America as whole, and is not specific to SCA.

This study investigates the atmospheric characteristics of ARs landfalling in SCA and the differences from ARs affecting latitudes farther north. This is accomplished first through an algorithm that detects AR activity by identifying plume-like features using reanalysis. Mechanisms associated with AR activity are examined with composites of various atmospheric variables for the identified AR events, organized by landfall region. Additionally, this study uses MJO and ENSO indices to describe the statistical significance of these phenomena over SCA landfalling ARs. This paper is organized as follows. Section 2 describes the datasets and methodologies used. Sections 3, 4, and 5 present the results of the validations, composites, and statistical analyses of the MJO and ENSO, respectively. Conclusions and implications are presented in Section 6.

2 Datasets and methods

We develop an algorithm to identify AR activity affecting North America’s west coast and particularly SCA based on an AR detection algorithm from Jiang et al. (2014). Daily total precipitable water (TPW) fields calculated from the National Oceanic and Atmospheric Administration’s (NOAA) National Centers for Environmental Prediction’s Climate Forecast System Reanalysis (CFSR) (Saha et al. 2010) at a 0.5° × 0.5° spatial resolution are used to identify AR events from 1979 to 2013. CFSR are used because of its high spatial resolution, the coupling to the ocean, and the assimilation of satellite radiances for the entire period of study (Saha et al. 2010). TPW (in kg m^{-2}) is an equivalent to integrated water vapor as it reflects the water total within an atmospheric column (vertically integrated, surface—200 mb) if all water vapor is condensed into liquid water with 1 $kgcm^{-2}$ equal to 1 mm (Campmany et al. 2010).

A previous record of AR activity created by Neiman et al. (2008a) and later extended by Dettinger et al. (2011) uses Special Sensor Microwave Imager (SSM/I) data to identify AR activity affecting North America’s west coast expanding water years 1998 to 2011. Here, we use TPW from reanalysis due to SSM/I’s limited temporal span. Extending the record

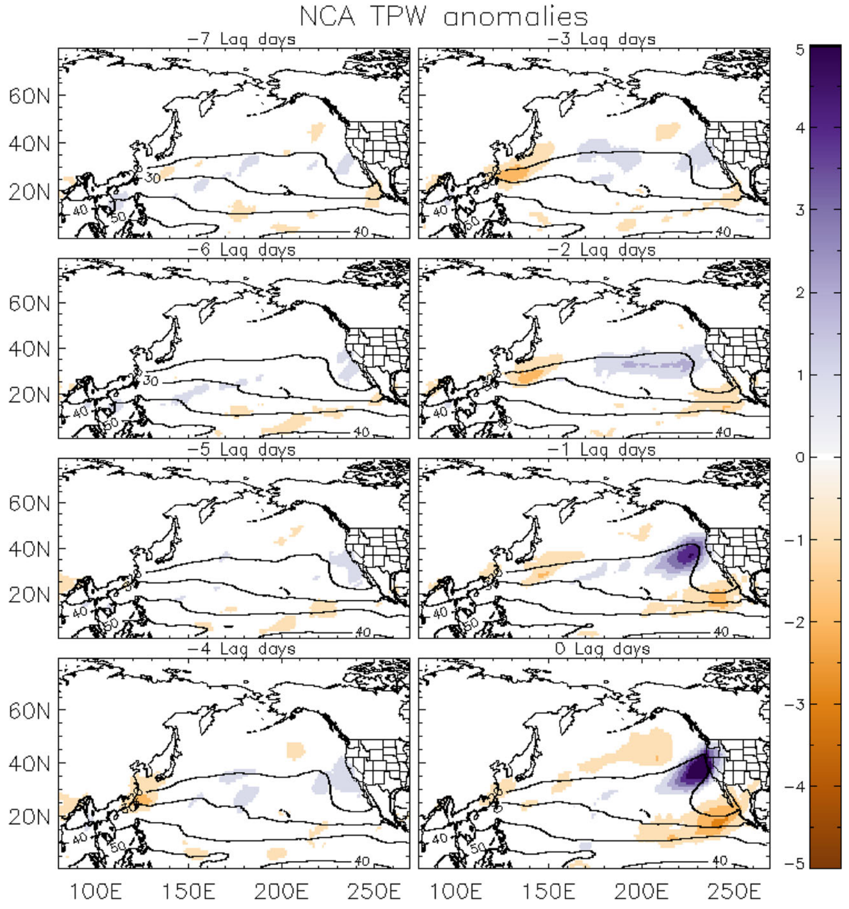

Fig. 4 Same as Fig. 3, but for ARs affecting NCA

provides additional AR cases (from 1979 to 2013) to adequately investigate the characteristics and dynamical forcings of these high-intensity episodes.

This algorithm modifies a previous AR detection procedure first introduced in Jiang and Deng (2011) and later modified in Jiang et al. (2014) that identifies AR plumes using the National Aeronautical and Space Administration's Modern Era Retrospective-Analysis for Research and Applications (MERRA) at a 0.5° latitude × 0.667° longitude spatial resolution. A summary of the tracking algorithm is described in steps 1–5 below. Note that steps 1–2 are based on Jiang et al. (2014) criteria while steps 3–5 describe the methodologies that were developed in the present study and differ from Jiang et al. (2014).

1. TPW grid point values (Q_r) north (south) of 15.0° N (15.0° S) that meet the following listed criteria are identified.

$$Q_r \geq Q_{z\text{mean}} + A\left(Q_{z\max} - Q_{z\text{mean}}\right) \tag{1}$$

$$Q_r \geq Q_{m\text{mean}} + B(Q_{m\max} - Q_{m\text{mean}}) \tag{2}$$

$$Q_r \geq q_{\text{cut}} = 20 \text{ mm} \tag{3}$$

where $Q_{z\text{mean}}$, $Q_{z\max}$, $Q_{m\text{mean}}$, and $Q_{m\max}$ refer to the zonal (latitudinal, z) and meridional (longitudinal, m) mean and max values of Q_r (i.e., TPW), respectively. Parameters A and B are meant to preserve the elongated shape of the AR and are identified as 0.3 and 0.1, respectively. Variable q_{cut} is a threshold parameter referring to the minimum TPW value required to be considered an AR (Jiang and Deng 2011; Jiang et al. 2014).

2. Of the identified Q_r points, contiguous areas meeting or exceeding an area threshold mark of 5.0×10^5 km^2 are determined and smaller regions are dismissed as they are considered too small to be ARs. Jiang et al. (2014) uses an area threshold of 2.5×10^5 km^{2}which we conclude is too small as it classifies extraneous filamentary features as ARs.
3. ARs exhibit elongated geometry. To identify the elongation of the AR candidates, we calculate the first two (orthogonal) eigenvectors (or principal components) that explain most of the spatial variance of each large contiguous region. The first two eigenvectors (PC-1 and PC-2, respectively) can be interpreted as the two axes of an ellipse that best fits to the area. From the ellipse axes, we are able to calculate eccentricity, defined as the ratio between the minor (PC-2) and major (PC-1) axes of the ellipse. This fit ellipse procedure is the most prominent

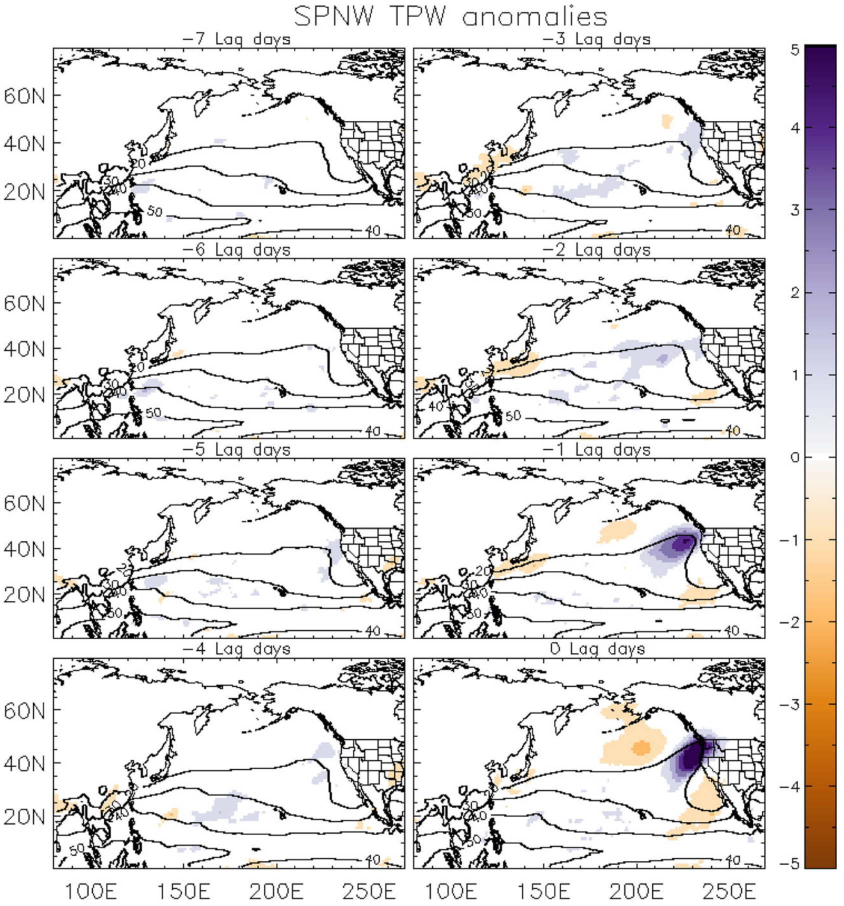

Fig. 5 Same as Fig. 3, but for ARs affecting SPNW

difference between this algorithm and the one described in Jiang et al. (2014) that uses an aerial fraction criterion to determine AR eligibility.

4. Ellipses with eccentricities less than 0.40 as well as widths less than 1000 km are classified as ARs. The 0.40 criterion is used to guarantee the AR's elongated structure. If the feature is greater than 1000-km wide, then the eccentricity must be less than 0.30. Although a width of 1000 km or less is used as a defining AR characteristic (e.g., Neiman et al. 2008a,b; Ralph et al. 2005, 2006, 2010; Zhu and Newell 1994, 1998), an AR may occur within a broader region of high TPW and using the 0.30 eccentricity criterion for wider TPW areas attempts to capture these features.
5. For all identified ARs, ellipse orientation is calculated using the first eigenvector (PC-1) and determining the degrees counter clockwise from the *x*-axis (east–west orientation). ARs affecting North America are often oriented between 0.0° and 90.0° due to the dominant wind patterns and Coriolis force. Features that meet all of the above criteria are defined as ARs landfalling along the western coast of North America.

Dates classified as ARs by the AR algorithm (steps 1–5) but not meeting a visual inspection of AR criteria are identified and removed so as not to skew composites. From the total record of 762 identified events, 43 are removed leaving 719 AR events. ARs are then categorized according to landfall region.

Even though SCA experiences high-intensity ARs responsible for significant proportions of regional annual precipitation (e.g., Dettinger et al. 2011; Kim et al. 2013; Rutz and Steenburgh 2012), fewer ARs occur in SCA compared to latitudes farther north (Neiman et al. 2008a,b; Rutz et al. 2014); therefore, it is important to determine if SCA ARs have unique characteristics. Additionally the orientation of much of SCA's coastline as well as a local mountain range, the Transverse Range, run in an east–west direction rather than the typical north–south common to the rest of western North America (Schoenherr 1992). This affects how storms make landfall and ultimately how they interact with the environment in this region. We conduct composite analyses to determine if the overall features of SCA ARs differ from other ARs. In the record from Neiman et al. (2008a) and Dettinger et al. (2011), AR activity affecting North America's west coast from 32.5° to 52.5° N is identified where the coast is divided into two domains "south-coast" (i.e., CA; 32.5°–41.0° N) and "north-coast" (i.e., Oregon, Washington, and/or British Columbia; 41.0°–52.5° N). To maintain

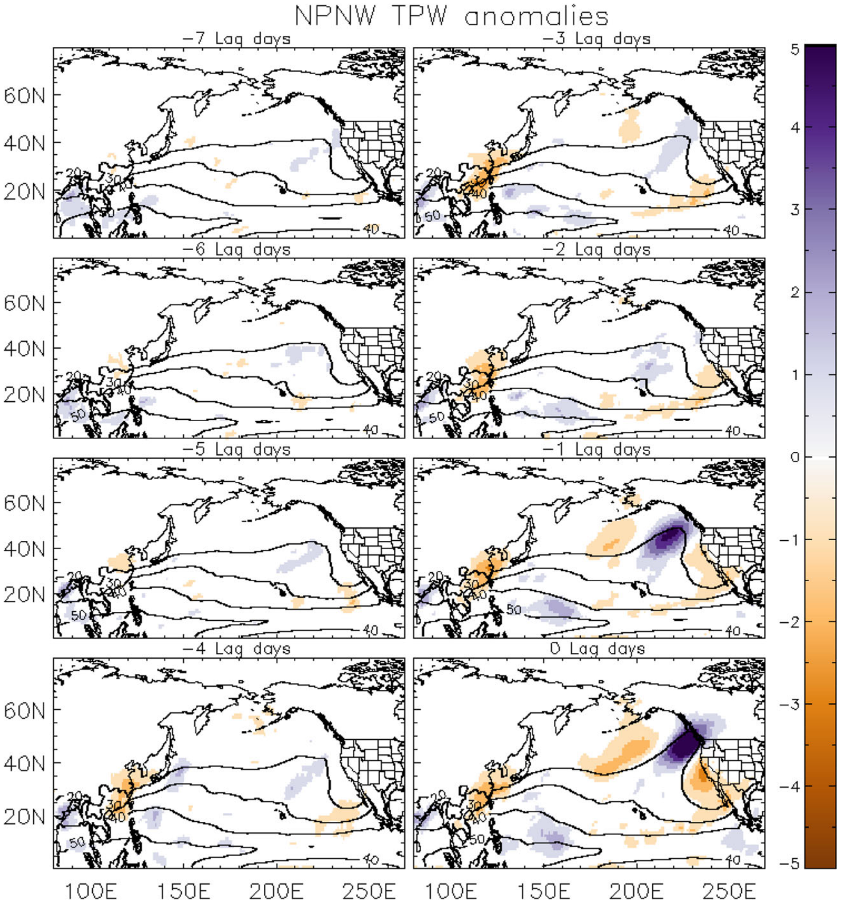

Fig. 6 Same as Fig. 3, but for ARs affecting NPNW

consistency with the previous record, composites are performed over the latitudinal domain of 32.5°–52.5° N. However, as we intend to investigate the role of ARs in SCA, the subdomains are partitioned into smaller groups. For simplicity, we divide the domain into four subdomains each with similar latitudinal ranges: SCA (32.5° ≤ latitude ≤ 37.0°), northern California (NCA, 37.0° < latitude ≤ 42.0°), Southern Pacific Northwest (SPNW, 42.0° < latitude ≤ 47.0°), and Northern Pacific Northwest (NPNW, 47.0° < latitude ≤ 52.5°). These ranges additionally capture the change of coastal and mountain orientation for SCA discussed earlier.

To perform a comprehensive analysis of AR features and identify AR characteristics according to region of landfall, lag composites of various atmospheric variables (from CFSR) are created for different landfalling regions for the dominant rainy season months of October through March (Oct–Mar). Lag composites are created from 10 days prior to the day of the event (0 Lag days) to 3 days after the AR landfall. Atmospheric variables examined include TPW, TPW anomalies, 500-mb geopotential heights (h500), h500 anomalies, as well as 2-m surface temperature (t2m) anomalies. Daily anomalies are calculated at each grid point by removing the smoothed annual cycle.

3 Validation and case studies

First, we assess the modified algorithm's ability to detect AR events compared to the algorithm identified in Jiang et al. (2014). We applied both algorithms using CFSR for the December, January, and February (DJF) months of 1979–2005 to obtain AR climatology according to latitude (between 30.0° and 55.0° N) (Fig. 1). Our algorithm (Fig. 1a) exhibits a peak of approximately 9% of all landfalling ARs affecting western North America at about 40° N whereas Jiang et al.'s (2014) algorithm (Fig. 1b) shows a peak of 8% around 39° N. The latitudinal variation of AR landfall probability is comparable between both methods with AR probability decreasing farther away from 40° N. However, our algorithm indicates a greater decrease in AR probability towards latitudes equatorward of 40° N compared to Jiang et al. (2014). For instance the AR landfall probability at 35° N drops to about 2.5% in our algorithm compared to 4.5% for Jiang et al. (2014). The regional AR climatology obtained with MERRA and discussed in Jiang et al. (2014) suggests a maximum AR probability of approximately 10% around 40° N for DJF 1979–2005 (see Jiang et al. 2014, Fig. 1), whereas our algorithm run using MERRA found approximately 8% of all landfalling ARs around 40° N and a similar profile (not shown).

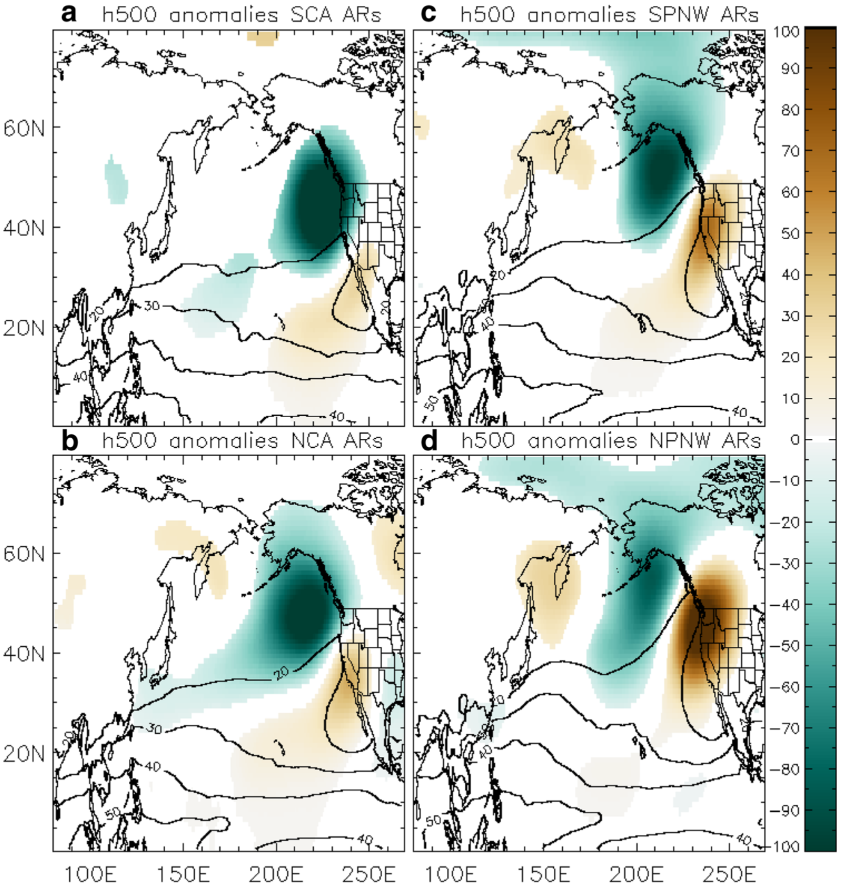

Fig. 7 Composites of h500 anomalies (*colored shading*; m) on the day of AR landfall (0 Lag days) for ARs affecting **a** SCA, **b** NCA, **c** SPNW, and **d** NPNW. Anomalies are calculated at the 95% level using a Student's *t* test. TPW contours are overlaid to help visualize AR plume location and begin at 20 kg m^{-2} with a contour interval of 10

Additionally, four independent AR dates affecting North America's west coast identified in previous analyses (Ralph and Dettinger 2012; Ralph et al. 2010) are examined using outputs from both algorithms with CFSR as inputs (Fig. 2). Case study dates include March 26, 2005, November 7, 2006, October 13, 2009, as well as December 18, 2010. Outputs of these dates are visually assessed in order to investigate how well each algorithm identifies AR features. Both identification algorithms detect all four ARs; still, differences between each set of outputs can be identified in terms of recognition of extraneous features not directly related to the investigated AR. For example, for March 26, 2005, an AR extending from the Hawaiian Islands northeastward to the Oregon coast is identified by both the modified algorithm (Fig. 2a) as well as the original algorithm (Fig. 2e). However, while the modified algorithm identifies this plume as the only feature affecting North America, the original algorithm identifies another component affecting the US east coast and the Gulf of Mexico. This feature may be associated with high TPW values from an existing storm. It is important that the algorithm does not identify these features as we want to eliminate characteristics that do not classify as ARs (such as the movement of the Monsoon, hurricanes, etc.). Overall, the modified algorithm (Fig. 2a–d) gives a more precise identification of AR plumes and excludes objects not directly related to the event of interest. This is most likely due to the criterion of eccentricity adopted in the modified method (step 3) as the first two eigenvectors accurately capture the elongated AR shape.

4 Synoptic characteristics

The numbers of independent AR events during Oct–Mar from 1979 to 2013 separated according to landfall regions are 72

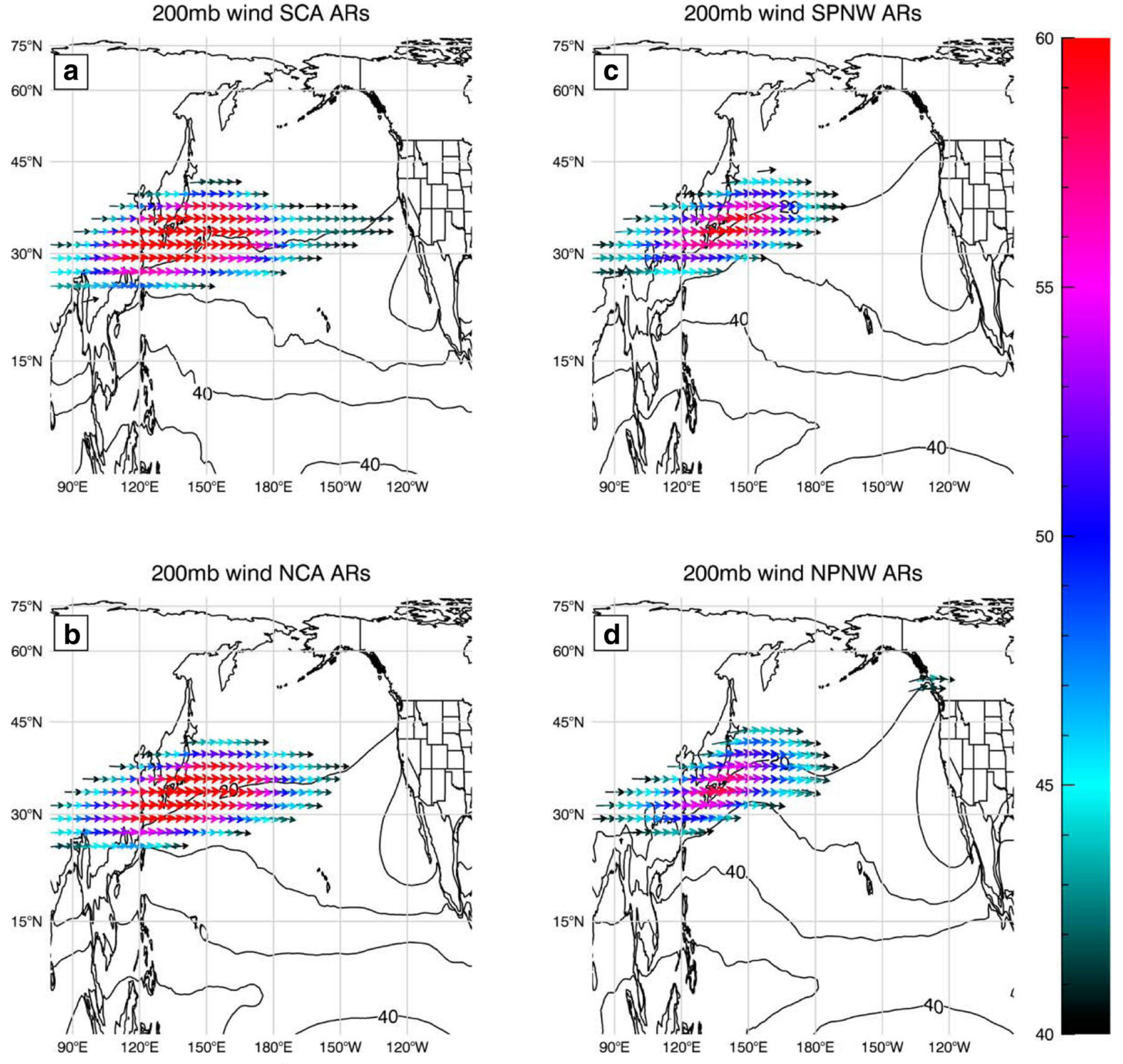

Fig. 8 Composites of 200-mb wind (ms^{-1}) on AR landfall days for ARs affecting **a** SCA, **b** NCA, **c** SPNW, and **d** NPNW. Winds below 40 ms^{-1} are disregarded in order to visualize the location of the jet core. TPW (contours) is overlaid to help visualize AR plume location

SCA, 213 NCA, 183 SPNW, and 160 NPNW (Table 1), in agreement with previous literature in that AR landfalls are greatest between northern California and southern Canada with decreased frequencies upon moving southward (e.g., Rutz et al. 2014). Independent events are defined as ARs with no other AR events within ±3 days of landfall. In spite of large year-to-year variability in the frequency of AR events (not shown), no significant trends in AR occurrence is observed for any of the investigated landfall regions during the examined time period (1979–2013). In SCA, there are several seasons with zero detected AR events. As AR storms bring about large proportions of SCA's annual rainfall totals (e.g., Dettinger et al. 2011; Kim et al. 2013; Rutz and Steenburgh 2012), a lack of these extreme events may lead to a severe reduction in seasonal rainfall totals.

The main objective of this study is to examine dynamical mechanisms associated with ARs affecting North America's west coast at different latitudes and particularly SCA. Figures 3, 4, 5, 6, 7, 8, 9, 10, 11 and 12 show composites of atmospheric variables for all landfall regions. ARs are characterized by baroclinic wave trains propagating through the Pacific resulting in northeastward extending moisture plumes (Neiman et al. 2008a). These plumes are flanked to the northwest and southeast by areas of dryness as indicated by anomalous TPW values that appear days prior to AR landfall with both positive and negative anomalies strengthening as an AR approaches landfall (Figs. 3, 4, 5, and 6). After landfall, moisture plumes retreat from the coast and dissipate (not shown).

Composites of TPW and TPW anomalies (Figs. 3, 4, 5, and 6) on AR landfall days (0 Lag days) for all landfall regions display, as expected, positive TPW anomalies within regions of high TPW (i.e., the AR moisture plume) with neighboring negative anomalies to the northwest and southeast, consistent with a midlatitude wave train pattern. These anomalies appear similar in terms of area covered for all regions. Additionally, all ARs display comparable maximum positive anomalies (+10 kg m^{-2} SCA, Fig. 3; +9 kg m^{-2} for all other landfall regions, Fig. 4, 5, and 6) as well as negative anomalies, including negative anomalies to the southeast of the AR plume (−6 kg m^{-2} SCA, Fig. 3; −3 kg m^{-2} NCA, Fig. 4; −2 kg m^{-2} SPNW, Fig. 5; −3 kg m^{-2} NPNW, Fig. 6). For all landfall regions, the strongest positive anomalies on AR landfall days appear offshore, near the coastline and do not stretch farther inland. As these are areas of mountainous terrain, it suggests that the topography impedes on AR progression possibly affecting AR persistence and intensity (Rutz et al. 2014).

Prior to landfall (Lag −7 to −1 days), ARs are associated with a buildup of moisture above the eastern Pacific Ocean that occurs a few days earlier (Figs. 3, 4, 5, and 6), characterizing

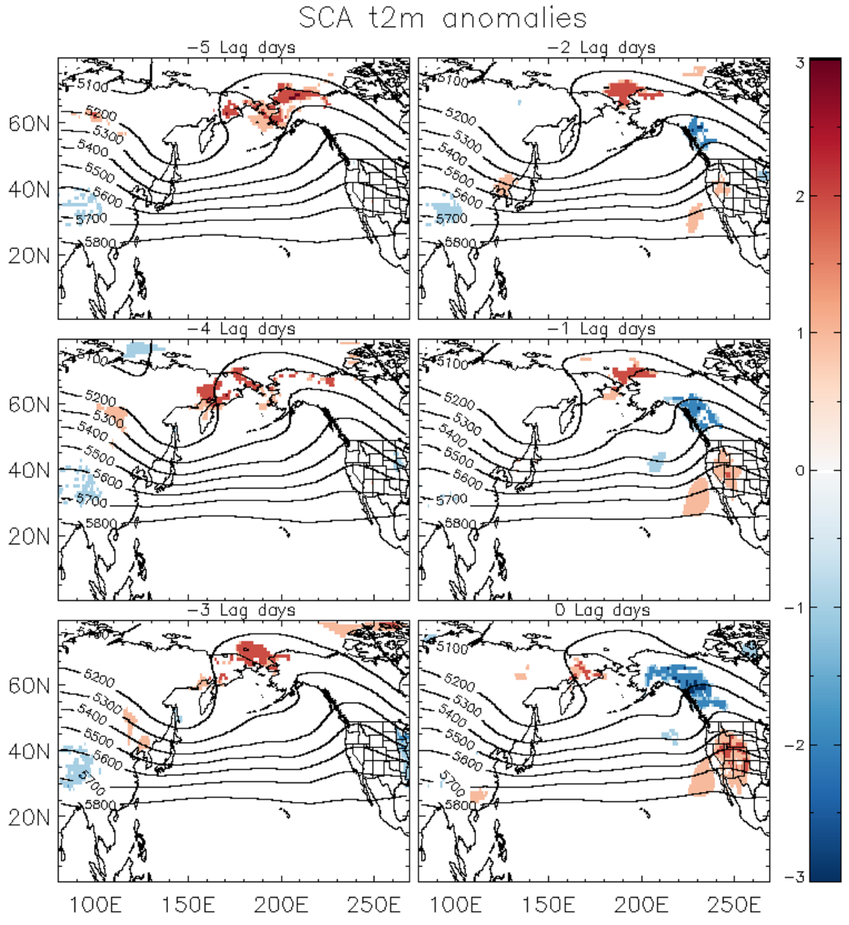

Fig. 9 Composites of t2m anomalies (*colored shading*; °C) and h500 (contours; m) starting 5 days prior to AR landfall (−5 Lag days) and continuing to the day of AR landfall (0 Lag days) for ARs affecting SCA. Anomalies are calculated at the 95% level using a Student's *t* test

Fig. 10 Same as Fig. 9, but for ARs affecting NCA

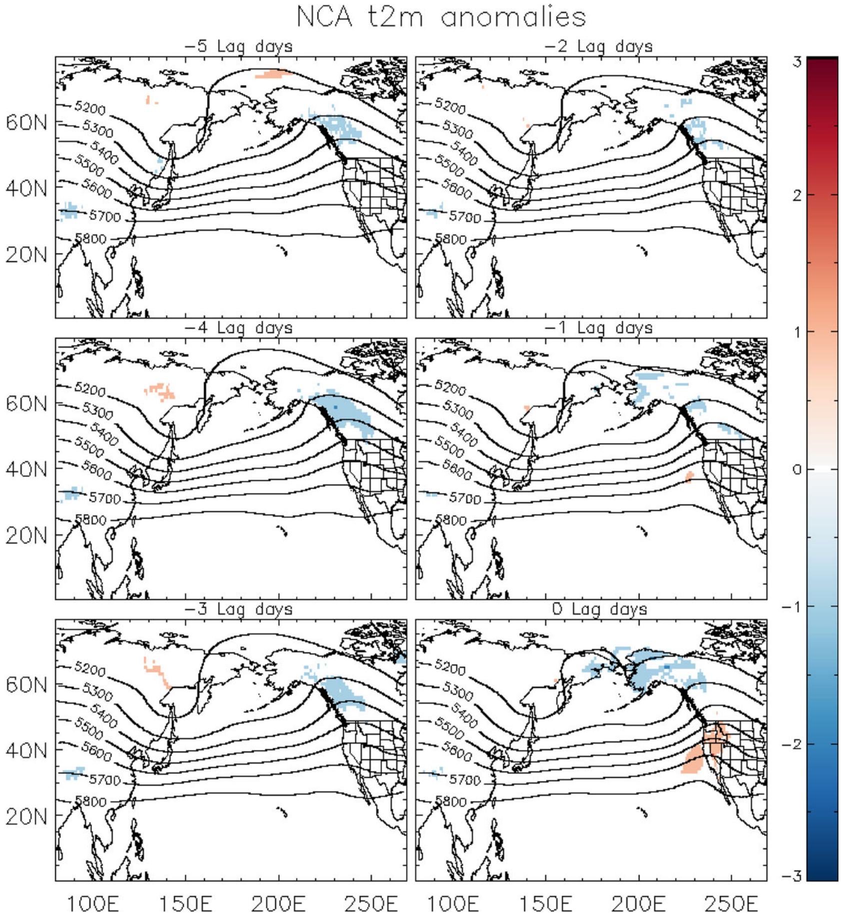

ARs as synoptic scale phenomena. As composites are averages of group events, weak or no statistically significant anomalies indicate case-to-case variability and suggest that SCA ARs have greater consistency among events due to statistically significant anomalies, whereas ARs landfalling farther north show more variability in the days prior to AR landfall. In other words, statistically significant anomalies resulting from the composites of these fields do not properly characterize the narrow zones with high TPW anomalies associated with ARs landfalling farther north. This is because of the spatial characteristics of the ARs and the large case-to-case variability of the moisture plumes. In terms of orientations, leading edges for SCA AR moisture plumes initialize farther eastward as well as equatorward with their trailing ends extending to the eastern Pacific (Fig. 3) whereas leading edges for ARs landfalling farther north initialize farther westward and poleward as well as have trailing ends extending farther westward (Figs. 4, 5, and 6). These orientation differences are as anticipated and suggest that SCA ARs vary in terms of manifestation as well as possible moisture sources from ARs landfalling farther north.

Composites of h500 anomalies (Fig. 7a–d) on AR landfall days display trough-ridge couplets with an offshore trough and onshore ridge leading to overall southwesterly flow for all landfall regions (Neiman et al. 2008a). SCA ARs exhibit the lowest positive h500 anomalies (maximum +34 m SCA, Fig. 7a) as well as the strongest negative anomalies (minimum −159 m) corresponding to the onshore ridge and offshore trough, respectively. These differences result in a shifting of the trough and ridge axes, guiding AR moisture farther south along the coastline. The other landfall regions have weaker negative h500 anomalies (minimum −118 m NCA, Fig. 7b; −107 m SPNW, Fig. 7c; −87 m NPNW, Fig. 7d) as well as stronger positive anomalies (maximum +49 m NCA; +72 m SPNW; +123 m NPNW), guiding wind and moisture farther northward along the coast. Additionally, SCA ARs are associated with negative h500 anomalies over Oregon, Washington, and southern British Columbia that are closer to the coast as well as positive anomalies to the south and southeast (Fig. 7a). These anomalies shift for ARs landfalling farther north with NPNW ARs displaying positive h500 anomalies over Oregon, Washington, and southern British Columbia with weaker negative anomalies directly to the south and west and additional positive anomalies off the coast of Hawaii (Fig. 7d). These h500 anomaly wave train patterns resemble the two phases of the Pacific/North American Teleconnection Pattern (PNA), with SCA ARs most closely resembling the negative PNA (PNA−) phase and NPNW resembling the positive PNA (PNA+) phase (Wallace and

Fig. 11 Same as Fig. 9, but for ARs affecting SPNW

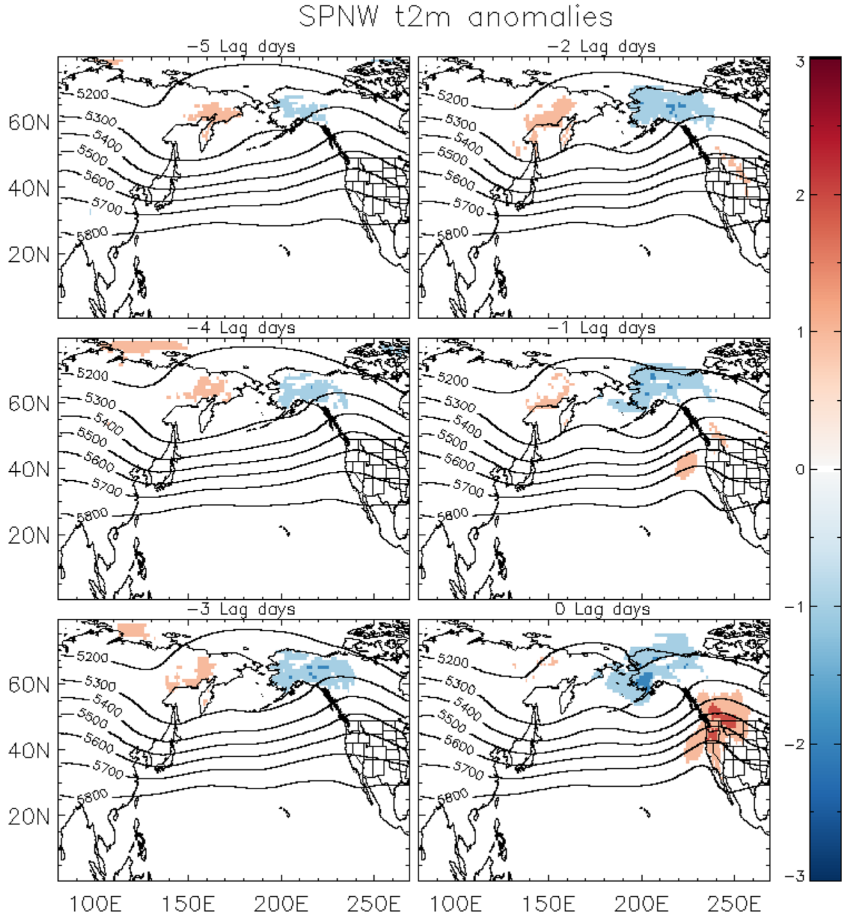

Gutzler 1981). PNA− involves a westward retraction of the jet stream along with cooler, wetter weather over western North America while PNA+ indicates an eastward extension of the jet stream along with warm, drier conditions over southwestern North America (Leathers et al. 1991).

A daily PNA record from NOAA's Climate Prediction Center (CPC) reveals a neutral trend in PNA occurrences during Oct–Mar 1979–2013 (not shown) with a slightly higher proportion of PNA+ events at or greater than 1 standard deviation, and an analysis of AR frequencies corresponding with PNA phases at or greater (less) than +1 (−1) standard deviation (Table 2) reveals greater AR incidences during PNA+ for all four landfall regions. However, according to a test of proportions at a 95% confidence interval, the frequency of SCA ARs during PNA+ is not significantly greater than that during PNA−, whereas ARs during PNA+ are significantly more frequent for all other landfall areas. A previous study by Guan et al. (2013) concludes that from Nov. 1997 to Mar. 2011, ARs affecting the Sierra Nevada are more frequent during PNA−. Although our results do not support this finding, it is important to note that the study of Guan et al. (2013) focuses on a smaller, mountainous area within eastern California and covers a shorter time span (1997–2011) during which the PNA was predominantly negative. In a different study, Payne and Magnusdottir (2014) determine that from 1979 to 2011 ARs affecting North America's west coast between 20.0° and 60.0° N are associated with a westward retraction of the jet stream which coincides with changes in the potential vorticity gradient resulting in Rossby wave breaking. Figure 8a–d shows composites of 200-mb winds on AR landfall days for each location. Only wind speeds meeting or exceeding a 40-ms^{-1} threshold are shown in order to visualize the upper level jet core. These composites show an eastward extension of the jet core for SCA ARs (Fig. 8a) whereas the jet core retracts farther westward for ARs landfalling farther north (Fig. 8b–d). Particularly, SCA ARs show more intense jets east of 180° E compared to SPNW and NPNW, and with NCA, SCA ARs showing more intense jet east of 150° W, closer to shore. As ARs landfall farther south, the jet core is more zonally oriented with greater concentrations of strong winds ($\geq 60\ \mathrm{ms}^{-1}$) and shifts to a more wavelike pattern as ARs landfall farther north. This displacement of the jet core suggests that while a westward retraction of jet winds is important for most ARs landfalling along the western coast of North America (consistent with results from Payne and Magnusdottir 2014), an eastward movement of the jet exit region plays a significant role with SCA ARs. Additionally, this retraction and extension may not be primarily determined by PNA phase.

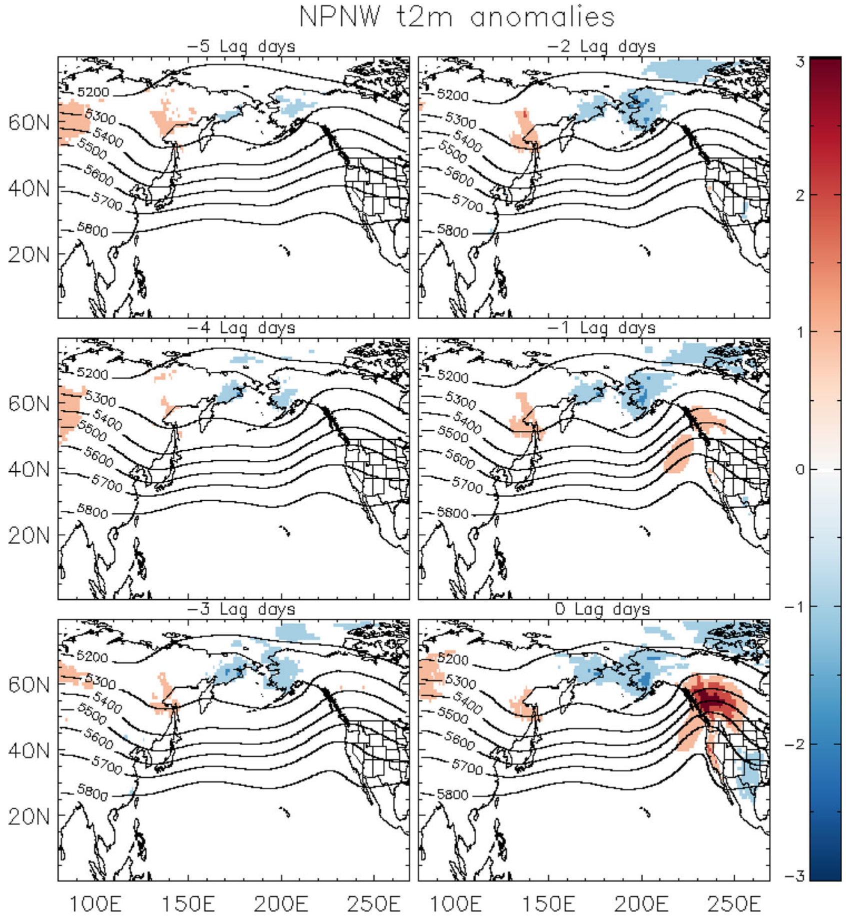

Fig. 12 Same as Fig. 9, but for ARs affecting NPNW

T2m anomaly composites (Figs. 9, 10, 11, and 12) for AR landfall days show warming within AR plumes for all landfall regions, consistent with findings that ARs have warm low troposphere temperatures (Neiman et al. 2008a). Additionally, warming is seen downstream of AR plumes confirming the presence of onshore ridges (Neiman et al. 2008a) whereas cooling is observed poleward of the plume. These patterns of temperature along with the corresponding geopotential height patterns are consistent with the baroclinic wave theory, supporting the idea that ARs are components of extratropical cyclones. Even though SCA ARs have the least amplified onshore ridge, positive t2m anomalies downstream of AR plumes are comparable to other landfall regions (+2 °C, SCA, Fig. 9; +2 °C, NCA, Fig. 10; +2 °C, SPNW, Fig. 11; +3 °C, NPNW, Fig. 12), suggesting dynamical forcing of SCA ARs.

Table 2 AR frequencies according to landfall region coinciding with strong (±1 standard deviation) positive and negative PNA phases

	No. ARs	PNA(+)	PNA(−)
SCA	72	15	10
NCA	213	62	18
SPNW	183	51	21
NPNW	160	42	6
All ARs	719	201	63

Prior to landfall, h500 composites (Figs. 9, 10, 11, and 12) show differing trough-ridge patterns progressing through the Pacific. Five days prior to landfall (−5 Lag days), all regions develop a trough over the far western Pacific near the Korean Peninsula along with a ridge over Alaska. However, the trough appears most pronounced for ARs landfalling farther south with SCA ARs (Fig. 9) displaying the widest trough as well as the most amplified ridge. The dynamics of these systems along with the previously described extension/retraction of jet winds suggest that the amplitude of the trough developing over eastern Asia/the western Pacific along with an adjacent amplified ridge is perhaps the main mechanism responsible for the equatorward displacement of upper level jet. This leads to the eastward extension of the jet core, forcing AR associated moisture to landfall farther south, eventually landfalling in SCA.

5 MJO and ENSO effects

AR occurrences at landfall coinciding with MJO activity are assessed using an MJO index from Jones and Carvalho (2012). This index identifies daily MJO activity including

MJO phases (p1–p8) and magnitudes. A complete description of the index and its construction can be found in Jones and Carvalho (2012). Of the 6370 dates examined (Oct–Mar 1979–2013), 3873 (60.8%) align with active MJO and 2497 (39.2%) with inactive MJO. For the 719 identified AR events landfalling on North America's west coast (30.0°–55.0° N) during Oct–Mar 1979–2013, 418 (58.13%) occur during an active MJO whereas 301 (41.86%) ARs take place during an inactive MJO (Table 3). For the 72 ARs landfalling in SCA, 40 (55.56%) occur during an active MJO and 32 (44.4%) during an inactive MJO. All landfall regions experience greater AR frequencies during active MJOs; however, for all regions except NPNW, the AR frequency differences during active and inactive MJO are not statistically significant according to a test of proportions at a 95% confidence interval. This suggests that for most of western North America during Oct–Mar, ARs landfalling during active MJO may occur by chance.

In regard to MJO phases (Table 4) for all landfalling ARs (30.0°–55.0° N), the greatest AR frequencies occur during p1 and p7 (62 dates each) with secondary peaks at p3 (58 dates) and p6 (54 dates). During p1, MJO enhanced convection manifests over the equatorial Indian Ocean with suppressed convection directly to the east over the western Pacific Ocean along with a retracted jet stream (Bell and Higgins 2005; Zhang 2005). At p3 enhanced convection has migrated eastward over the eastern Indian Ocean with suppressed convection towards the central Pacific. By p6, enhanced convection has continued to the western equatorial Pacific Ocean with suppressed convection directly to the west over the equatorial eastern Indian Ocean. At p7, enhanced convection has progressed farther towards the central Pacific Ocean and begins to dissipate, while wind and surface pressure signals normally coupled with the convection continue to propagate eastward and suppressed convection is to the west over the western Pacific Ocean (e.g., Jones and Carvalho 2012). Additionally, as the MJO enhanced convection advances towards the central Pacific, there is an eastward extension of the Jet Stream (Bell and Higgins 2005; Zhang 2005). Overall AR activity is consistent with previous analyses such as from Guan et al. (2012) who states that SWE fractions in the Sierra Nevada from ARs increase during MJO p3 and p6.

Table 3 AR frequencies according to landfall region during active (ac.) and inactive (in.) MJO

	No. ARs	MJO (ac.)	Percent	MJO (in.)	Percent
SCA	72	40	55.56	32	44.44
NCA	213	133	62.44	80	37.56
SPNW	183	115	62.84	68	37.16
NPNW	160	81	50.63	79	49.38
All ARs	719	418	58.14	301	41.86

Table 4 AR frequencies according to landfall region corresponding to various MJO phases

	p1 (phase1)	p2	p3	p4	p5	p6	p7	p8
SCA	4	9	6	2	7	3	6	3
NCA	15	16	16	16	12	19	28	11
SPNW	21	18	17	12	13	13	10	11
NPNW	15	6	11	13	10	12	11	3
All ARs	62	52	58	50	47	54	62	33

Additionally, Payne and Magnusdottir (2014) conclude that ARs affecting North America's west coast (20.0° –60.0° N) increase during MJO p3, p6, p7, and p8, with the greatest frequency increase during p6. However, our results show half the total ARs during p8. Conclusions from individual landfall regions (Table 4) are inconsistent with these previous findings and are also not uniform between landfall areas suggesting that MJO activity during particular MJO phases is not indicative of specific AR landfall location.

AR events at landfall and coinciding ENSO phases are also assessed. ENSO phases are identified from the Oceanic Niño Index (ONI) from the CPC of NOAA. A description of ONI's construction can be found at the CPC's website (www.cpc.ncep.noaa.gov). For all identified ARs (30.0°–55.0° N) during Oct–Mar 1979–2013, the greatest event frequencies occur during neutral ENSOs (315 dates, 43.8%) with roughly even numbers during warm (203 dates, 28.2%) and cold (201, 28.0%) ENSOs (Table 5). As neutral ENSO occurs most frequently (45.2% of Oct–Mar 1979–2013, with 29.0% warm and 25.7% cold), this is to be expected. NCA, SPNW, and NPNW ARs also occur more frequently during neutral ENSO conditions (Table 5). However, SCA ARs show more even proportions of warm (25, 34.72%), cold (25, 34.72%), and neutral (22, 30.56%) ENSOs (Table 5) that is significant according to a test of proportions at the 95% confidence interval. This is also apparent in Fig. 13 that shows AR interannual variability by water year for each landfall location. The increased frequencies of ARs during ENSO neutral conditions for NCA, SPNW, and NPNW are consistent with previous findings from Bao et al. (2006). Payne and Magnusdottir (2014) conclude that during warm ENSOs AR landfalling

Table 5 AR frequencies according to landfall region corresponding to ENSO phases

	No. ARs	Warm	Percent	Cold	Percent	Neutral	Percent
SCA	72	25	34.72	25	34.72	22	30.56
NCA	213	53	24.88	60	28.17	100	46.95
SPNW	183	51	27.87	53	28.96	79	43.17
NPNW	160	48	30.00	42	26.25	70	43.75
All ARs	719	203	28.23	201	27.96	315	43.81

Fig. 13 Seasonal Oct–Mar AR frequencies for water years 1980–2013 and corresponding ENSO phase during landfall for **a** SCA, **b** NCA, **c** SPNW, and **d** NPNW

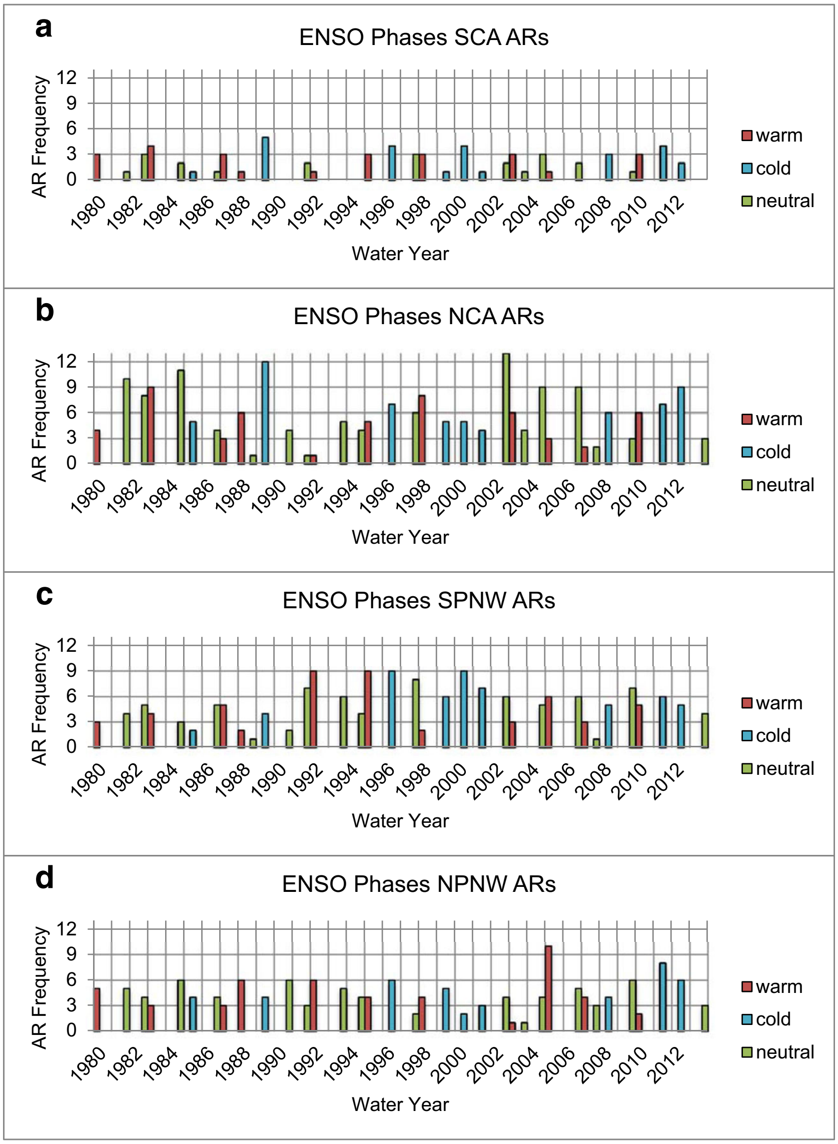

latitudes shift southward, in part explaining the increase of AR frequencies in SCA during warm ENSOs but not the frequency increase during cold ENSOs. These results indicate that the ENSO neutral phase may provide the background atmospheric conditions required for AR occurrence in western North America but may not play a direct role in the development and/or modulation for ARs occurring farthest south.

6 Conclusions

Understanding the characteristics and atmospheric conditions behind SCA AR events is imperative for proper forecasting, hazard mitigation, as well as water resources management. This study uses an algorithm to identify ARs affecting western North America within CFSR TPW fields spanning from 1979 to 2013 and then classifies ARs according to region of landfall. The current identification method modifies of a previous algorithm established by Jiang and Deng (2011) as well as Jiang et al. (2014) and most notably uses a fit ellipse approach to detect individual AR events. The algorithm identifies 719 ARs landfalling between 30.0° and 55.0° N with 72 landfalling in SCA, 213 in NCA, 183 in SPNW, and 160 in NPNW. Composites of TPW, TPW anomalies, h500, h500 anomalies, 200-mb winds, as well as t2m anomalies are investigated for ARs affecting each individual landfall region on the day of, prior to, and after AR landfall in order to differentiate characteristics of ARs landfalling in different areas. In general, ARs landfalling along the North American west coast are characterized by baroclinic midlatitude wave trains progressing through the Pacific resulting in northeastward oriented moisture plumes extending from low to midlatitudes that appear to culminate along coastal mountain ranges. On landfall days, ARs are characterized by an offshore trough and onshore ridge as well as localized low tropospheric warming.

Although SCA ARs display similar features to ARs landfalling farther north along the western coast of North America, differences arise in their progression and landfall. Anomalously high moisture associated with AR plumes appears farther eastward as well as equatorward for SCA ARs and in addition, materialize days earlier suggesting that SCA AR moisture plume patterns have less case-to-case variability. Several days prior to landfall, SCA ARs display a wide trough off the eastern coast of Asia along with an amplified ridge over Alaska leading to the displacement and possible merger of the upper level jets and subsequent eastward extension of the jet core with winds at or greater than 60 ms^{-1} close to shore. In combination with an offshore trough and weak onshore ridge on the day of landfall, there is increased zonal flow of wind and moisture suggesting that the region of landfall depends on the phase, position, and amplitude of the wave train.

ARs occurring during and throughout various phases of the PNA, MJO, and ENSO are also investigated with SCA ARs again exhibiting differing relationships than that of ARs landfalling farther north. h500 anomalies for SCA ARs most closely resemble PNA− whereas ARs landfalling farther north resemble PNA+. However, an analysis of ARs with the PNA index indicates that ARs occur more frequently during PNA+ for all landfall regions but that the frequencies of SCA ARs during PNA+ and PNA− is not significantly different. All other landfall regions show significantly increased AR activity during PNA+. This finding is contradicted by the eastward extension of the jet core seen with SCA ARs, a feature associated with PNA+, suggesting that other mechanisms may be more relevant in modifying the position of the jet. Additionally, as ARs landfall farther north, there is a westward retraction of the jet core, a feature more common to the PNA− phase. This indicates that the PNA may not be the main driver of AR activity for the western coast of North America.

The frequencies of SCA, NCA, and SPNW ARs reveal no statistically significant differences of proportions for active or inactive MJO whereas NPNW ARs occur more evenly between active and inactive MJO, inconsistent with overall MJO activity. Furthermore, while ARs in general occur more frequently during MJO phases 1, 3, 6, and 7, when separated into landfall regions, there is no discernible pattern. In regard to ENSO, SCA ARs occur evenly between warm, cold, and neutral ENSOs whereas NCA, SPNW, and NPNW see greater AR frequencies during ENSO neutral conditions in accordance with ENSO proportions. These results hint at the complexity of SCA ARs, as the dominant mechanisms affecting ARs along the North American western coast do not appear to affect SCA ARs the same way.

Acknowledgements The authors greatly appreciate many helpful discussions with Charles Jones who was crucial to the algorithm's development. The availability of CFSR data as well as ONI and PNA indices from NOAA was very helpful. Sarah M. Harris is grateful for financial support from the University of California Graduate Division.

References

Bao JW, Michelson SA, Neiman PJ, Ralph FM, Wilczak JM (2006) Interpretation of enhanced integrated water vapor bands associated with extratropical cyclones: their formation and connection to tropical moisture. Mon Wea Rev 134:1063–1080

Bell GD, Higgins W (2005) National Oceanic and Atmospheric Administration, Climate Prediction Center. 18 December 2004–17 January 2005: U.S. Storms and Flooding in the West and Midwest Exceptional Warmth in the Midwest and East. Climate Prediction Center Web. http://www.cpc.ncep.noaa.gov/products/expert_assessment/california_assessment_2005.pdf 23 February 2016

Caine N (1980) The rainfall intensity: duration control of shallow landslides and debris flows. Geogr Ann Ser A: Phys Geogr 62:23–27

Campmany E, Bech J, Rodríguez-Marcos J, Sola Y, Lorente J (2010) A comparison of total precipitable water measurements from radiosonde and sunphotometers. Atm Res 97:385–392

Dettinger MD (2004) Fifty-two years of pineapple-express storms across the West Coast of North America. California Energy Commission PIER Energy-Related Environmental Research Report CEC-500-2005-004, p 15

Dettinger MD, Ralph FM, Das T, Neiman PJ, Cayan DR (2011) Atmospheric rivers, floods, and the water resources of California. Water 3:455–478

Guan B, Waliser DE, Molotch NP, Fetzer EJ, Neiman PJ (2012) Does the Madden-Julian oscillation influence wintertime atmospheric rivers and snowpack in the Sierra Nevada? Mon Wea Rev 140:325–342

Guan B, Molotch NP, Waliser DE, Fetzer EJ, Neiman PJ (2013) The 2010/11 snow season in California's Sierra Nevada: role of atmospheric rivers and modes of large-scale variability. Water Resour Res 49:6731–6743

Jiang T, Deng Y (2011) Downstream modulation of North Pacific atmospheric river activity by East Asian cold surges. Geophys Res Lett 38:L20807. doi: 10.1029/2011GL049462

Jiang T, Evans KJ, Deng Y, Dong X (2014) Intermediate frequency atmospheric disturbances: a dynamical bridge connecting western U.S. extreme precipitation with East Asian cold surges. J Geophys Res: Atmospheres 119:3723–3735. doi: 10.1002/2013JD021209

Jones C (2000) Occurrence of extreme precipitation events in California and relationships with the Madden–Julian oscillation. J Clim 13:3576–3587

Jones C, Carvalho LMV (2012) Spatial-intensity variations in extreme precipitation in the contiguous United States and the Madden-Julian oscillation. J Clim 24:4898–4913

Jones C, Gottschalck J, Carvalho LMV, Higgins W (2011) Influence of the Madden-Julian oscillation on forecasts of extreme precipitation in the contiguous United States. Mon Wea Rev 139:332–350

Kim J, Waliser DE, Neiman PJ, Guan B, Ryoo J-M, Wick GA (2013) Effects of atmospheric river landfalls on the cold season precipitation in California. Clim Dyn 40:465–474. doi: 10.1007/s00382-012-1322-3

Knippertz P, Martin JE (2007) A Pacific moisture conveyor belt and its relationship to a significant precipitation event in the semiarid southwestern United States. Wea Forecasting 22:125–144. doi: 10.1175/WAF963.1

Leathers DJ, Yarnal B, Palecki MA (1991) The Pacific/North American teleconnection pattern and United States climate. Part I: Regional temperature and precipitation associations. J Clim 4:517–528

Madden RA, Julian PR (1994) Observations of the 40-50-day tropical oscillation—a review. Mon Wea Rev 122:814–837

Mo KC, Higgins RW (1998) Tropical influences on California precipitation. J Clim 11:412–431

Neiman PJ, Ralph FM, White AB, Kingsmill DE, Persson POG (2002) The statistical relationship between upslope flow and rainfall in California's coastal mountains: observations during CALJET. Mon Wea Rev 130:1468–1492

Neiman PJ, Ralph FM, Wick GA, Lundquist JD, Dettinger MD (2008a) Meteorological characteristics and overland precipitation impacts of atmospheric rivers affecting the west coast of North America based on eight years of SSM/I satellite observations. J Hydrometeorol 9:22–47

Neiman PJ, Ralph FM, Wick GA, Kuo YH, Wee TK, Ma Z, Taylor GH, Dettinger MD (2008b) Diagnosis of an intense atmospheric river impacting the Pacific Northwest: storm summary and offshore vertical structure observed with COSMIC satellite retrievals. Mon Wea Rev 136. doi:10.1175/2008MWR2550.1

Neiman PJ, Schick LJ, Ralph FM, Hughes M, Wick GA (2011) Flooding in western Washington: the connection to atmospheric rivers*. J Hydrometeorol 12. doi:10.1175/2011JHM1358.1

Neiman PJ, Ralph FM, Moore BJ, Hughes M, Mahoney KM, Cordeira JM, Dettinger MD (2013) The landfall and inland penetration of a flood-producing atmospheric river in Arizona. Part I: Observed synoptic-scale, orographic, and hydrometeorological characteristics. J Hydrometeorol 14:460–484

Newman M, Kiladis GN, Weickmann KM, Ralph FM, Sardeshmukh PD (2012) Relative contributions of synoptic and low-frequency eddies to time-mean atmospheric moisture transport, including the role of atmospheric rivers. J Clim 25. doi:10.1175/JCLI-D-11-00665.1

Payne AE, Magnusdottir G (2014) Dynamics of landfalling atmospheric rivers over the North Pacific in 30 years of MERRA reanalysis. J Clim 27. doi:10.1175/JCLI-D-14-00034.1

Ralph FM, Dettinger MD (2011) Storms, floods, and the science of atmospheric rivers. Eos, Trans Amer Geophys Union 92:265–272

Ralph FM, Dettinger MD (2012) Historical and national perspectives on extreme west coast precipitation associated with atmospheric rivers during December 2010. Bull Amer Meteor Soc 93:783–790

Ralph FM, Neiman PJ, Wick GA (2004) Satellite and CALJET aircraft observations of atmospheric rivers over the eastern North Pacific Ocean during the winter of 1997/98. Mon Wea Rev 132:1721–1745

Ralph FM, Neiman PJ, Rotunno R (2005) Dropsonde observations in low-level jets over the northeastern Pacific Ocean from CALJET-1998 and PACJET-2001: mean vertical-profile and atmospheric-river characteristics. Mon Wea Rev 133:889–910

Ralph FM, Neiman PJ, Wick GA, Gutman SI, Dettinger MD, Cayan DR, White AB (2006) Flooding on California's Russian River: role of atmospheric rivers. Geophys Res Lett 33. doi:10.1029/2006GL026689

Ralph FM, Neiman PJ, Kiladis GN, Weickmann K, Reynolds DW (2010) A multi-scale observational case study of a Pacific atmospheric river exhibiting tropical–extratropical connections and a mesoscale frontal wave. Mon Wea Rev 139. doi:10.1175/2010MWR3596.1

Rutz JJ, Steenburgh WJ (2012) Quantifying the role of atmospheric rivers in the interior western United States. Atm Sci Lett:13. doi:10.1002/asl.392

Rutz JJ, Steenburgh WJ, Ralph FM (2014) Climatological characteristics of atmospheric rivers and their inland penetration over the western United States. Mon Wea Rev 142:905–921

Rutz JJ, Steenburgh WJ, Ralph FM (2015) The inland penetration of atmospheric rivers over western North America: a lagrangian analysis. Mon Wea Rev 143. doi:10.1175/MWR-D-14-00288.1

Saha S, Moorthi S, Pan HL, Wu X, Wang J, Nadiga S, Tripp P, Kistler R, Woollen J, Behringer D, Liu H, Stokes D, Grumbine R, Gayno G, Wang J, Hou YT, Hy C, Juang HMH, Sela J, Iredell M, Treadon R, Kleist D, Van Delst P, Keyser D, Derber J, Ek M, Meng J, Wei H, Yang R, Lord S, van den Dool H, Kumar A, Wang W, Long C, Chelliah M, Xue Y, Huang B, Schemm JK, Ebisuzaki W, Lin R, Xie P, Chen M, Zhou S, Higgins W, Zou CZ, Liu Q, Chen Y, Han Y, Cucurull L, Reynolds RW, Rutledge G, Goldberg M (2010) The NCEP climate forecast system reanalysis. Bull Am Meteorol Soc 91:1015–1057

Schoenherr AA (1992) A natural history of California, vol 56. Univ of California Press, pp 8

Sodemann H, Stohl A (2013) Moisture origin and meridional transport in atmospheric rivers and their association with multiple cyclones*. Mon Wea Rev 141:2850–2868

Wallace JM, Gutzler DS (1981) Teleconnections in the geopotential height field during the Northern Hemisphere winter. Mon Wea Rev 109:784–812

Zhang C (2005) Madden-Julian oscillation. Rev Geophys 43:1–26

Zhu Y, Newell RE (1994) Atmospheric rivers and bombs. Geophys Res Lett 21:1999–2002

Zhu Y, Newell RE (1998) A proposed algorithm for moisture fluxes from atmospheric rivers. Mon Wea Rev 126:725–735